



HAL
open science

Experimental and CFD investigation of inert bed materials effects in a high-temperature conical cavity-type reactor for continuous solar-driven steam gasification of biomass

Houssame Boujjat, Sylvain Rodat, Srirat Chuayboon, Stéphane Abanades

► To cite this version:

Houssame Boujjat, Sylvain Rodat, Srirat Chuayboon, Stéphane Abanades. Experimental and CFD investigation of inert bed materials effects in a high-temperature conical cavity-type reactor for continuous solar-driven steam gasification of biomass. *Chemical Engineering Science*, 2020, 228, pp.115970. 10.1016/j.ces.2020.115970 . hal-02929996

HAL Id: hal-02929996

<https://hal.science/hal-02929996>

Submitted on 4 Sep 2020

HAL is a multi-disciplinary open access archive for the deposit and dissemination of scientific research documents, whether they are published or not. The documents may come from teaching and research institutions in France or abroad, or from public or private research centers.

L'archive ouverte pluridisciplinaire **HAL**, est destinée au dépôt et à la diffusion de documents scientifiques de niveau recherche, publiés ou non, émanant des établissements d'enseignement et de recherche français ou étrangers, des laboratoires publics ou privés.

1 **Experimental and CFD investigation of inert bed materials effects in a high-**
2 **temperature conical cavity-type reactor for continuous solar-driven steam**
3 **gasification of biomass**

4 Houssame Boujjat^{1,2}, Sylvain Rodat³, Srirat Chuayboon³, Stéphane Abanades^{3*}

5 ¹*CEA-LITEN Solar and Thermodynamic Systems Laboratory (L2ST), F-38054 Grenoble, France*

6 ²*Univ. Grenoble Alpes, F-38000 Grenoble, France*

7 ³*Processes, Materials and Solar Energy Laboratory, PROMES-CNRS, 7 Rue du Four Solaire, 66120*
8 *Font-Romeu, France*

9 *Corresponding author: stephane.abanades@promes.cnrs.fr

10
11
12 **Abstract:** Solar biomass gasification was performed in a high-temperature conical bed reactor for
13 thermochemical syngas production, which represents an efficient route to promote biomass valorization
14 while storing intermittent solar energy into carbon-neutral solar fuels. The developed solar reactor is
15 based on a conical cavity-type receiver enabling continuous biomass feedstock injection under real
16 concentrated solar irradiation. In this study, the use of inert bed materials is considered to directly absorb
17 a portion of the entering solar power and to transmit thermal energy to the gas and reactive particulate
18 phase by radiation, convection and particle-to-particle interactions, with the aim of homogenizing the
19 reactor temperature. A fluid dynamics study of the gas/particle flow was first performed to provide
20 insights into the reactor hydrodynamics in the case of empty cavity and cavity containing inert particles in
21 the forms of packed-bed and spouted-bed. The beneficial effect of the inert particles bed was emphasized.
22 The spouted bed particles play a role in retaining the reacting biomass particles longer inside the reaction
23 zone and promote phase mixing, as also confirmed by cold tests on a replicated transparent mockup
24 cavity. Different inert particle bed materials were then considered and experimentally tested to unravel
25 their impact on the biomass conversion, syngas composition and yield, and gasification performance in
26 the solar-heated reactor operated at 1200°C and 1300°C.

27 **Keywords:** Solar energy, gasification, biomass, syngas, solar fuel, spouted-bed reactor.

28

29 **1. Introduction**

30 Over the last few decades, the interest in biomass gasification has increased due to the growing demand
31 for reducing global greenhouse gas emissions responsible for global warming (Safarian et al., 2019).
32 Major advantages of biomass gasification over combustion include its potential to produce different forms
33 of energy, fuels and chemicals. In conventional industrial autothermal gasification reactors, at least 30%
34 of the initial feedstock is burnt to supply the required heat (Higman, 2013). This reduces the complete use
35 of the biomass for fuel production and leads to the contamination of syngas by combustion by products.
36 The use of concentrated solar power (CSP) to drive the endothermal gasification reactions results in
37 saving biomass resources, thus producing more syngas with a higher quality while avoiding combustion,
38 thereby eliminating the need for downstream gas processing and pollutants abatement. Concentrated high-
39 flux solar energy systems (e.g., solar beam-down (Noone et al., 2012) and solar towers (Li et al., 2015))
40 can be used to achieve high gasification temperatures ($>1200^{\circ}\text{C}$), which favours the reactions kinetics and
41 tars thermal cracking, while being suitable to convert a wide variety of biomass feedstock types.

42 Solar thermochemical reactors generally depend on the method of heating the solid reactants. Directly
43 irradiated solar gasifiers generally make use of a transparent window that allows the concentrated sunlight
44 to enter directly the reaction chamber. In such configuration, efficient solar absorption is achieved and
45 heat losses are lowered, which enables to reach and maintain high temperatures (1000–1500 °C) (Puig-
46 Arnavat et al., 2013). However, the transparent window mechanical resistance and cleanness are
47 restraining factors due to inherent limitations regarding pressure and particles/smoke soiling/deposition
48 (Loutzenhiser et al., 2017). Alternatively, indirectly irradiated solar reactors use an opaque heat transfer
49 wall to capture the highly concentrated solar flux and then transfer it to the reaction zone, thus avoiding
50 the need for a transparent window. The type of material selected for the emissive wall should be
51 constrained by its resistance to thermal shocks and maximum operating temperature, while it should offer
52 chemical inertness, radiative absorbance, high thermal conductivity, and suitability for transient
53 operation. The first solar gasifier (Gregg et al., 1980) was a directly irradiated fixed bed reactor and was
54 successful to convert different carbonaceous materials into syngas with more than 40% of the incoming
55 sunlight effectively stored as fuel value in the product gas. Taylor et al. (1983) studied a directly
56 irradiated fixed bed reactor for charcoal, wood and paper gasification. This reactor was irradiated from
57 the top and the charge was pushed upwards the focal point using a piston as the gasification progressed.
58 The obtained performance was compared to that of a directly irradiated fluidized bed reactor for CO_2
59 charcoal gasification. Compared to its fixed bed equivalent, which has an energy efficiency of 40%, the
60 fluidized bed reactor reached only 10% efficiency at 950°C because of the more pronounced radiation
61 losses on the upper part of the reactor and additional sensible losses in the exit gas. Piatkowski et al.
62 (2009) studied another fixed bed reactor with batch mode operation. This reactor was indirectly irradiated
63 using a solar simulator and was used to convert a wide variety of carbonaceous waste feedstocks such as

64 scrap tire powder, industrial sludge and sewage sludge. The main drawback of this reactor was its very
65 low conductive heat transfer rate that entailed significant temperature gradients and impaired the
66 conversion throughout the bed. Kodama et al. (2002) gasified bituminous coal with CO₂ in a small-scale
67 fluidized bed reactor directly irradiated by a Xe lamp from the side. The fluidized coal particles were in
68 direct contact with the quartz window, which was detrimental to its cleanliness and mechanical integrity.
69 Therefore, in another study, the concept was improved by developing a new solar fluidized bed reactor
70 irradiated from the top to insure a gap between the window area and the reacting particles (Kodama et al.,
71 2010). This fluidized bed reactor was further improved (Gokon et al., 2012) by adding a draft tube in the
72 centre of the reactor, which allowed homogenizing the temperature throughout the bed. Entrained and
73 vortex flow reactors were also solarized, and tested under both direct and indirect heating modes.
74 Z'Graggen et al. (2006) studied directly irradiated petroleum coke steam-gasification. The vortex flow
75 configuration allowed achieving up to 87% of petcoke conversion in a single pass of 1s residence time. In
76 the same vein, Müller et al. (2017) gasified charcoal-water slurry in a windowless indirectly irradiated
77 SiC cavity reactor at elevated pressure ranging from 1 to 6 bar. A reaction extent of 94% was obtained in
78 less than 5s with an upgraded calorific value of the feedstock of 35%. Other reactor designs were
79 investigated such as two-zone drop tube/packed bed reactors (Bellouard et al., 2017a; Kruesi et al., 2013)
80 where a porous material was placed in the hot region of the reactor to increase the particles residence time
81 in the reaction zone, and molten salt reactors (Hathaway et al., 2014) in which molten salt was used as
82 both heat transfer medium and catalyst for the reaction.

83 The present study was undertaken following the results of a previous work (Boujjat et al., 2019a,b) in
84 which a novel 1.5 kW_{solar} dilute solar spouted bed reactor was simulated and experimentally studied for
85 the first time. In the preceding work, the reactor was initially empty and the continuously injected
86 biomass particles were the only spouted particles inside the cavity. Such technology was suitable to
87 continuously convert the biomass feedstock with a high carbon conversion efficiency (~80%), and the
88 efficient storage of solar energy in the form of a readily transportable fuel was confirmed. With the
89 support of 3D multiphysics modelling, improvement strategies were proposed to enhance the phase
90 mixing, to limit the finest char particles entrainment and to homogenize the reactor temperature. The use
91 of inert particles (set at the bottom of the conical cavity in the form of spouted or packed-bed) appeared to
92 be judicious to achieve higher reaction extents and heat transfer rates. Therefore, in the present work,
93 different inert bed materials were tested for the first time to study their impact on the allothermal (solar-
94 only) continuous gasification of wood particles. Prior to the experimental study, the gas/particles flow
95 dynamics at real processing condition was investigated using Computational Fluid Dynamics (CFD)
96 modelling. Two thermal CFD models were developed on ANSYS-Fluent v19.1 to simulate the flow
97 through the inert packed and spouted bed particles in interaction with radiation and gas. These
98 simulations were completed by cold tests on a replicated transparent PMMA (Polymethyl methacrylate)
99 cavity mockup to validate the CFD predictions (at ambient temperature) and confirm the effective mixing

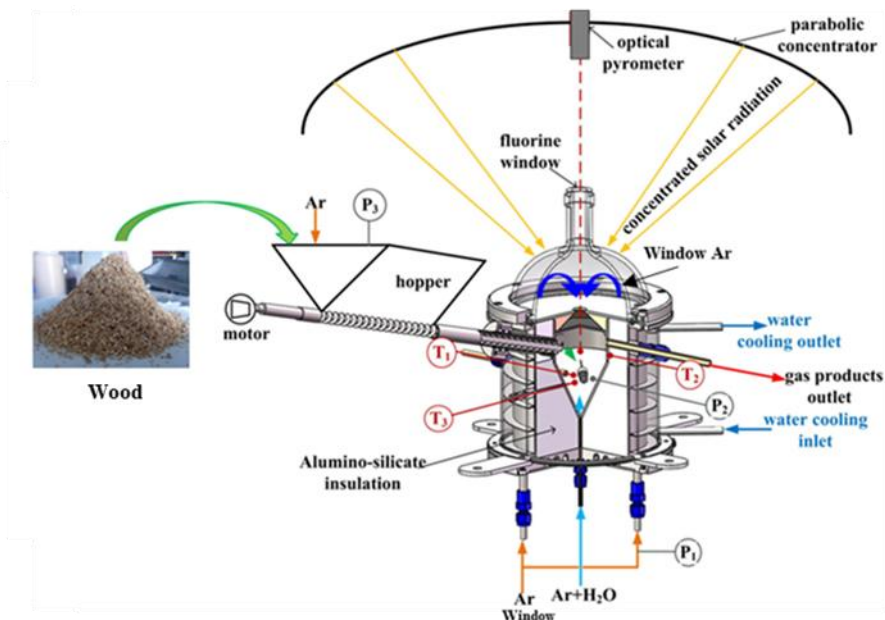
100 of the wood and bed particles. Thereafter, high temperature solar experiments were carried out at the
101 CNRS-PROMES solar furnace under real direct concentrated solar flux. Results in terms of syngas yield,
102 composition, biomass conversion and reactor performance metrics were discussed in light of the
103 numerical simulations.

104

105 2. Experimental set up

106 2.1 Solar reactor

107 The solar reactor was settled at the focus of a vertical-axis parabolic facedown concentrator (Supporting
108 Information, Figure S11). The reactor was based on the principle of conical spouted beds (Figure 1).
109 Being conical at the bottom and cylindrical in the upper free board region, a high velocity inlet fluid flow
110 expands the bed, and then spouts the central particles from the bottom to the upper fountain (Bellouard et
111 al., 2017b, 2018). A systematic circulation pattern is achieved in the upward direction through the spout
112 and slowly downward in the annulus region. Spouted bed reactors have been developed for various
113 applications including drying (Markowski and Kaminski, 1983), pyrolysis (Makibar et al., 2012) and non-
114 solar gasification (Lopez et al., 2017). Previous works on gasification have revealed the interests of
115 spouted beds over conventional fluidization for converting cohesive and sticky particles of various sizes,
116 shapes, densities, and textures (Erkiaga et al., 2013; Mathur and Gishler, 1955; Olazar et al., 1992,
117 Chuayboon et al., 2018a,b).



118

119 **Figure 1.** Scheme of the solarized conical dilute spouted bed reactor

120

121 Table 1 summarizes the main reactor materials and their physical properties. The cavity receiver was
122 consisting of a vertical cylinder (78 mm inside diameter) with a 60° angle conical bottom (total cavity

123 height: 115 mm) and was made of a high-temperature resistant metallic alloy (FeCrAl). The bottom inlet
 124 of the cavity was used for injecting the spouting gas via an alumina tube of 2 mm inside diameter from
 125 which the oxidizing agent (water steam) was fed. A layer (30 mm-thick) of porous ceramic fiber
 126 (aluminosilicate) was used to insulate the whole cavity. An alumina cap (20 mm-diameter aperture) was
 127 placed above the metallic cavity to maximize incoming absorbed solar radiation while reducing heat
 128 losses. A layer of zirconia felt (2 mm thickness) and a protective graphite plate were placed above the
 129 alumina cap to protect it from the direct high-flux solar radiation and minimize radiation losses. A
 130 stainless steel screw feeding system coupled with a hopper was used to transport the feedstock directly
 131 into the cavity. The whole feeding system was hermetically fixed to the water-cooled reactor shell.

132

133 **Table 1.** Reactor materials and properties (at 1400°C otherwise specified)

Component	Density ρ (kg.m ⁻³)	Heat capacity c_p (J.kg ⁻¹ .°C ⁻¹)	Thermal conductivity λ (W.m ⁻¹ .°C ⁻¹)
Alumina cap	4000	795	7
FerCrAl alloy	7100	800	35
Insulation	400	800	0.22
Zirconia layer	5700	500 (25°C)	2.2 (20°C)
Graphite layer	1400	710 (25°)	25 (25°C)

134

135 **2.2 Methods**

136 The gasified beech wood particles had an average diameter of 1 mm (Figure 2). Their characteristics are
 137 summarized in Table 2. They were obtained from XP CEN/TS 15104, XP CEN/TS 15105, XP CEN/TS
 138 15107, XP CEN/TS 14775 standards. Oxygen content was deduced by difference. The LHV (dry basis)
 139 was measured with a PARR 6200 bomb calorimeter knowing humidity from NF EN 14774 standard.
 140 Granulometry was obtained using a FT4 granulometer.

141

142 **Table 2.** Biomass composition and properties

C (wt.%)	H (wt.%)	O (wt.%)	N (wt.%)	S (wt.%)	Ash (wt.%)	Moisture (wt.%)	Density (kg.m ⁻³)	Specific heat (J.kg ⁻¹ .°C ⁻¹)	LHV (MJ.kg ⁻¹)
48.3	6.7	44.4	0.1	<0.1%	0.46	8.9	650	1500	16.93

143 The feedstock was stored in a 1.15L hopper and was continuously injected by the screw feeder. The wood
144 particles were transported into the hot cavity receiver and fell by gravity until complete injection of the
145 loaded biomass particles.

146 A flow of Ar (0.5 NL/min) was continuously injected via the hopper through the feeder, so that the hot
147 gases from the cavity could not interact with the reactive biomass feedstock. Moreover, to avoid window
148 fouling and overheating, a protective Ar flow (2 NL/min) was constantly flowed below the window for
149 sweeping and ensuring that all the product gases are directed to the reactor outlet. The jet gases (a mixture
150 of Ar carrier gas and steam) were injected from the alumina tube at the cavity bottom. The composition
151 (0.2 NL/min of Ar and 200 mg/min of steam) was adjusted to provide a slightly over-stoichiometric
152 Steam-to-Biomass (S/B) ratio.

153
154 The produced gases flowed through a bubbler and two cartridge filters to eliminate excess steam and
155 entrained char particles. An on-line gas analyzer (GEIT 3100) was used to continuously monitor the
156 syngas molar composition. The H₂ mole fraction was measured by a thermal conductivity detector (TCD)
157 while the mole fractions of CO, CO₂, and CH₄ were quantified by non-dispersive infrared detectors
158 (NDIR) (accuracy of measuring cells: ±2% of full scale, scales: 0-20% for H₂ and CO, 0-10% for CO₂
159 and CH₄). In addition, a gas chromatograph (GC) equipped with two columns (using Ar as carrier gas)
160 was used to measure the gas species concentrations and to specifically analyze the light hydrocarbons
161 (C₂H_m). Three temperature sensors (Pt-Rh thermocouples) were settled to monitor the reactor
162 temperatures (Figure 1). They were related to the inner temperature within the cavity volume (T₃ in the
163 conical region near the cavity bottom and T₁ at the cavity center) and to the external wall of the cavity
164 (T₂). The sensors tips were shielded by an alumina tube to protect them from the reacting gases. In
165 addition, a solar-blind pyrometer (Impac, operating at 4.8–5.2 μm in a H₂O absorption band) placed
166 above the reactor was used to measure the temperature at the cavity central core. Moreover, to ensure that
167 the reactor was maintained at an operating pressure below 1 bar (atmospheric pressure of 860 hPa due to
168 site elevation), a Venturi pump was placed at the outlet tube. A pressure measurement (P) was settled in
169 the cavity to monitor pressure variations throughout the experiments. All the obtained data were
170 controlled and collected by an automated data acquisition system (BECKHOFF).

171

172 **2.3 Bed materials**

173 Previous simulations using 3D CFD multiphysics modelling of the reactor (without bed materials)
174 (Boujjat et al., 2019a,b) revealed that the cavity wall temperature was 100°C higher than the inner
175 reaction zone temperature because of the direct absorption of most of the incoming radiations by the
176 cavity wall. Moreover, the lightest particles were entrained early towards the outlet by the high velocity
177 jet, which penalized the biomass conversion and syngas yields. Notable gradients in both steam
178 concentration and gas temperature between the central spout region and the annular zone were also

179 pointed out by the model, leading to strong variations in the particles conversion rate. With the aim of
 180 achieving higher reactor performance and better use of solar energy, inert bed materials set in the form of
 181 spouted or packed bed were considered. The spouted flow regime is expected to increase the reaction
 182 zone temperature and enhance the gas/wood particles phase mixing. The packed-bed configuration is used
 183 to broaden the gas stream at the cavity bottom, which should reduce the central gas jet velocity (thus
 184 increasing the gas residence time) and limit the entrainment of the reacting particles, when compared with
 185 an empty cavity configuration. Figure SI2 provides an illustration of the three studied hydrodynamic
 186 configurations.

187

188 Table 3 presents the tested packed and spouted particles characteristics.

189

Table 3. Inert particles characteristics at 1400°C

	Alumina (Al ₂ O ₃)	Silicon carbide (SiC)	Olivine	Silica sand (SiO ₂)
Density, ρ_s (kg.m ⁻³)	3950	3210	3270	1442
Thermal conductivity, λ_s (W.m ⁻¹ .°C ⁻¹)	7	15	0.6	2.2
Heat capacity, $c_{p,s}$ (J.kg ⁻¹ .°C ⁻¹)	795	1320	1220	1225
Mean diameter, d_s (mm)	3.00 or 0.12	0.30	0.30	0.20

190

191 The olivine main compounds included MgO, SiO₂, CaO (0.4% max) and Fe₂O₃. The mass fractions in
 192 Mg, Si and Fe were respectively 28.5%, 17.5% and 7%. Both SiC and olivine particles were thermally
 193 treated at 1000°C in presence of air to ensure inertness regarding the biomass thermochemical reactions
 194 of pyrolysis and gasification. Figure 2 shows a photography of the different particles.



Figure 2. Studied inert bed and wood biomass particles

195

196

197 **3. Modelling**

198 Prior to the high temperature experiments, multiphysics simulations of three configurations (empty
 199 cavity, inert packed-bed and spouted-bed particles) were performed to analyze the gas/solid flow behavior
 200 under real processing conditions using the same bottom and upper (window) gas flow rates as
 201 experiments with a solar power input of 900W. The reactor geometry was elaborated to closely represent
 202 the real reactor design (composed of different zones: alumina cap, insulation, cavity walls, and fluid / gas
 203 injection, reaction and exit zones). The geometry was meshed using an optimal cell size to accurately
 204 solve the gradients in the central spout region of the reactor where sharp variations in terms of
 205 temperature, gas velocity, and species mole fraction occur (Boujjat et al., 2019a). Two thermal CFD
 206 models were developed. The first one simulated the fluid flow through the porous packed bed. In this
 207 model, the packed bed particles were modelled through a momentum sink, which was function of the
 208 permeability and the porosity of the medium. A blending between the energy of fluid and solid particles
 209 was considered for the governing transport equation determining the temperature in the packed bed
 210 region. The model also allowed tracking discrete char particles in space by solving in a Lagrangian
 211 reference frame the discrete particles momentum and energy equations. The second model used the
 212 Eulerian-Eulerian (granular) approach to simulate the directly irradiated spouted bed particles. The flow
 213 was therefore described by conservation equations written for each phase separately (gas and granular).
 214 The endothermal pyro-gasification reaction was modelled by a volumetric heat sink applied to the fluid
 215 region of the cavity. Momentum, energy and radiative intensity transport equations used in the modelling

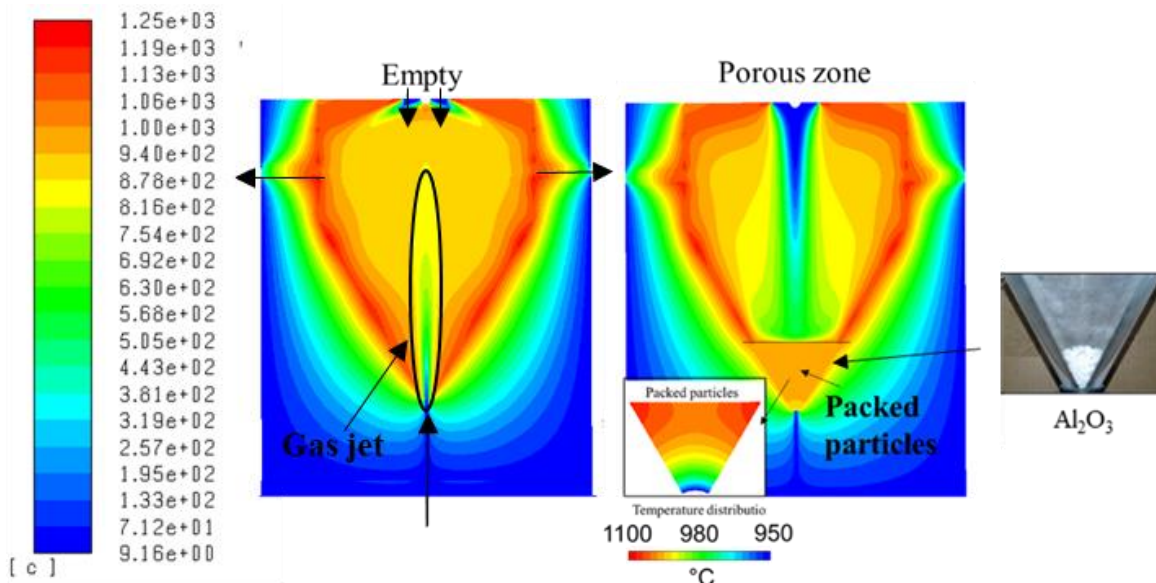
216 of the packed and the spouted powders are provided in detail in Tables SII-2. The reactor geometry, mesh
217 and boundary conditions are also presented in the Supporting Information (Section 2.1).

218

219 4. Results and discussion

220 4.1 Hydrodynamic & thermal study

221 The empty and the packed-bed configurations were simulated without discrete particles injection. Figure
222 3 shows the temperature field inside the solar reactor for a solar power input of 900W. It was observed
223 that for the two configurations, the cavity walls reached an average temperature of around 1230°C while
224 the gas phase average temperature was around 930°C. The empty cavity was characterized by a central
225 gas jet reaching a temperature of around 700°C at the center of the conical part of the cavity, which was
226 relatively colder than the annular region. In the packed bed configuration, the gas phase temperature
227 reached the same temperature (around 700°C) above the porous medium due to the cold window inlet Ar
228 flow rate. The porous zone model allowed to simulate heat transfer through the porous packed bed
229 (composed of 3mm particles). Accordingly, the bed top surface temperature was estimated at 1000°C at
230 its center and approached 1100°C nearby the cavity walls. Due to the thermal resistance of the packed
231 particles, and to the cooling of the bottom of the bed by the entering cold gases, the bed bottom
232 temperature was lower (around 950°C).



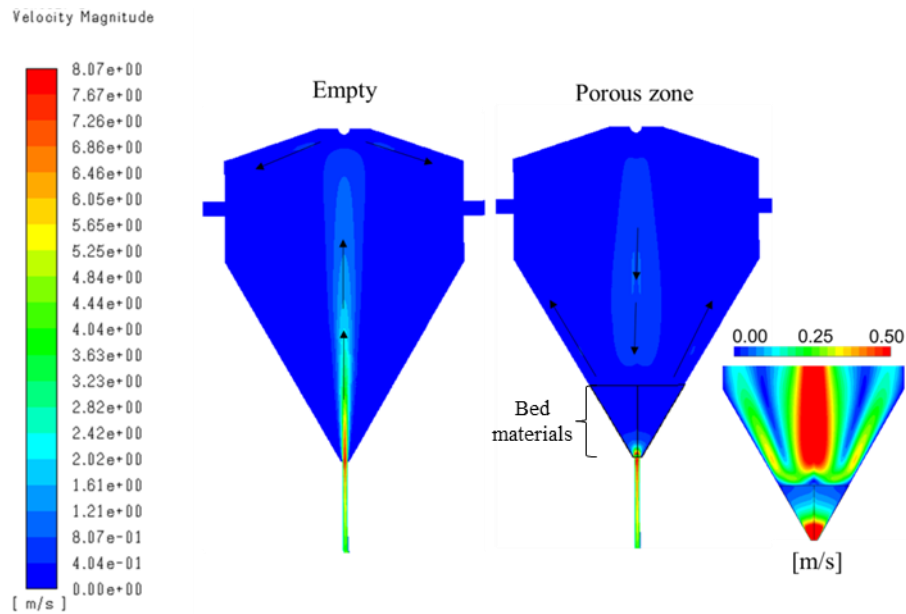
233

234

Figure 3. Temperature distribution: empty vs. packed bed

235

236 The gas velocity magnitude field inside the reactor is presented in Figure 4.



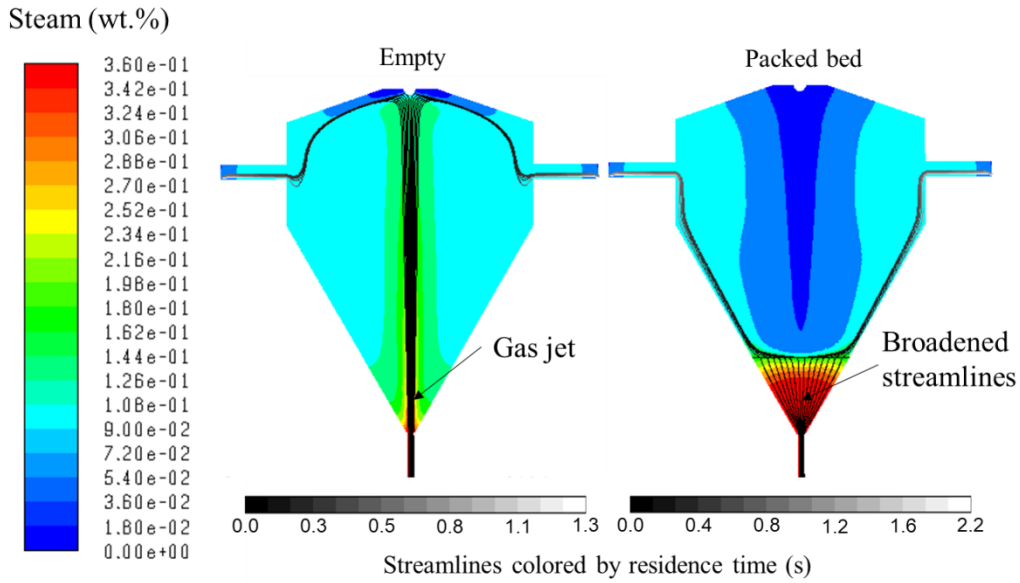
237

238

Figure 4. Velocity magnitude field: empty vs. packed bed

239

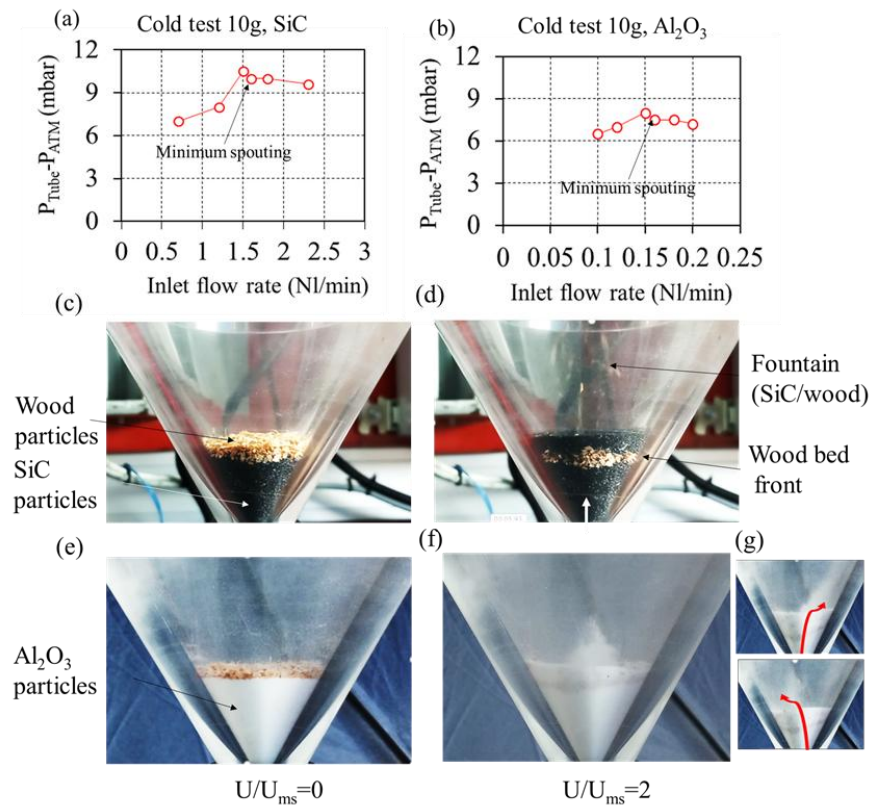
240 The simulations revealed a significant attenuation of the inlet gas flow velocity when using the packed
 241 particles. The gas jet velocity at the cone entrance was about 8 m/s. It then decreased to less than 0.5 m/s
 242 just above the bed. The Ar flow from the top of the reactor flowed downward to hit the bed top surface
 243 with a velocity of around 0.3m/s. It then flowed with the inlet gases towards the outlet along the cavity
 244 walls. The steam distribution inside the reactor and the inlet gas (water steam+argon) pathlines for the
 245 two configurations are presented in Figure 5. In the empty configuration, the central cavity region
 246 exhibited the highest water steam concentration, whereas the packed bed broadened the inlet gas
 247 streamlines over the entire cavity section, suggesting improved homogenization of chemical kinetics in
 248 the whole cavity region.



249
250
251

Figure 5. Steam distribution and inlet gas streamlines

252 The spouted bed configuration was studied at cold and at real processing conditions. Prior to the CFD
253 simulations, cold tests were carried out at ambient conditions with air on a transparent PMMA cavity
254 mockup to visualize the mixing of the particles and determine the minimum spouting conditions. The
255 obtained results for a 10g bed of SiC and Al₂O₃ particles are summarized in Figure 6.



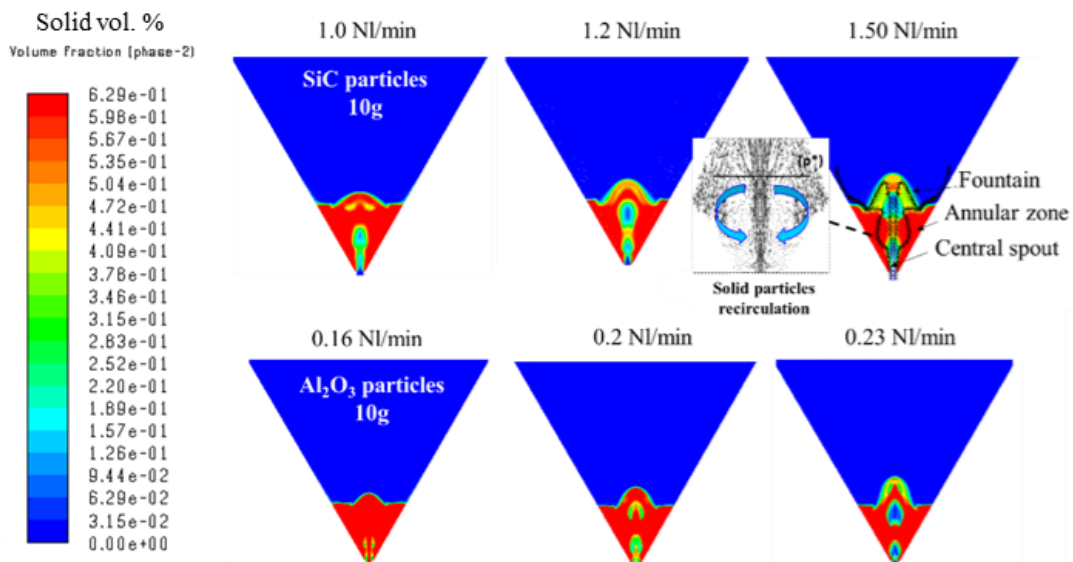
256
257

Figure 6. Experimental cold tests on a replicated PMMA cavity mockup (10g of inert particles)

258 The bed minimum spouting velocity was determined by plotting the bed pressure drop as function of the
 259 inlet gas flow rate. Figures 6-a,b show the measured pressure drop vs. the air flow rate for a 10g bed of
 260 300 μm SiC and 125 μm Al_2O_3 particles. It can be observed that by increasing the gas flow rate, the total
 261 pressure drop increased until reaching a maximum value that initiated the spouting of the particles
 262 (around 11 mbar for SiC and around 8 mbar for Al_2O_3 bed). Accordingly, minimum spouting flow rates
 263 of 1.5 NI/min ($v_{\text{exp,SiC}}=7.42$ m/s) and 0.16 NI/min ($v_{\text{exp,Al}_2\text{O}_3}=0.85$ m/s) were measured for the SiC and
 264 Al_2O_3 particles. In Figures 6-c to 6-f, a thin layer of wood particles was set at the top of the inert bed to
 265 visualize the stirring of the wood particles for $U/U_{\text{ms}} \sim 2$. A very stable spouting regime and well-ordered
 266 mixing of the particles was observed with the SiC particles, whereas the Al_2O_3 particles showed 3D
 267 instabilities that distorted the central gas jet path. As a result, the fountain height was constantly varying
 268 and changing its position, as illustrated in Figure 6-g. This undermined the particles recirculation from the
 269 top of the bed to the bottom. Such spouting instabilities were observed in previous studies (Olazar et al.,
 270 1992) and were due to different interdependent factors such as too large or too small cone angles. They
 271 could also occur when the height of the bed exceeded the maximum spoutable height, or when the
 272 spouted powders diameter was too small to be fluidized in a coherent and stable fashion.

273 These results were compared to 2D axisymmetric CFD simulations using the Eulerian approach. Figure 7
 274 shows the spouted bed particles space distribution for different inlet gas flow rates.

275

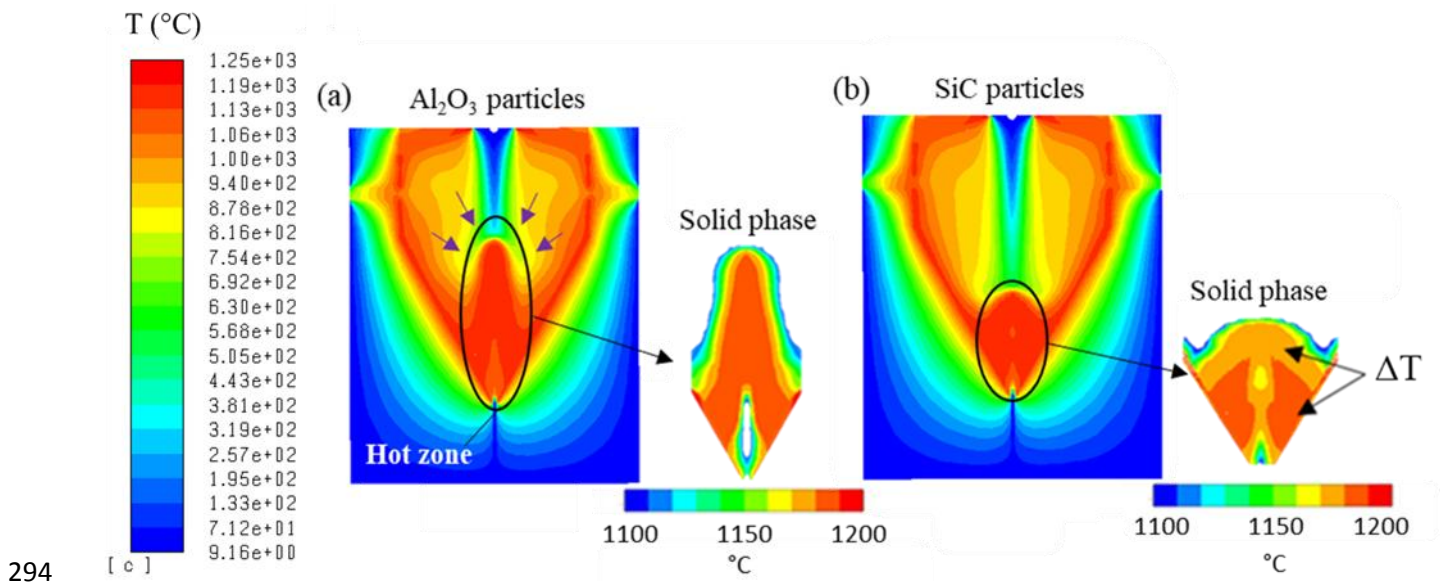


276
 277 **Figure 7.** Spouted bed particles space distribution for different inlet air flow rates (10g of inert particles,
 278 $t=2\text{s}$)

279 The cyclic particle-flow recirculation pattern through the three distinct regions (central spout, annular
 280 zone and fountain above the bed surface) was well reproduced by the Eulerian model. The predicted
 281 minimum spouting flow rate was 1.5 NI/min for the SiC bed ($v_{\text{sim,SiC}}=7.95$ m/s) and 0.23 NI/min for the

282 Al_2O_3 bed ($v_{\text{sim},\text{Al}_2\text{O}_3}=1.22$ m/s). These predictions were in agreement with the experimentally measured
 283 values for SiC within an error range of 4% and slightly overestimated the minimum spouting flow rate by
 284 about 0.07 Nl/min for the Al_2O_3 particles. The observed discrepancies for the Al_2O_3 particles can be due
 285 to the aforementioned flow perturbations (Figure 6-g) that potentially facilitated the gas passage through
 286 the annular region. Such 3D instabilities could not be reproduced by the 2D axisymmetric model.

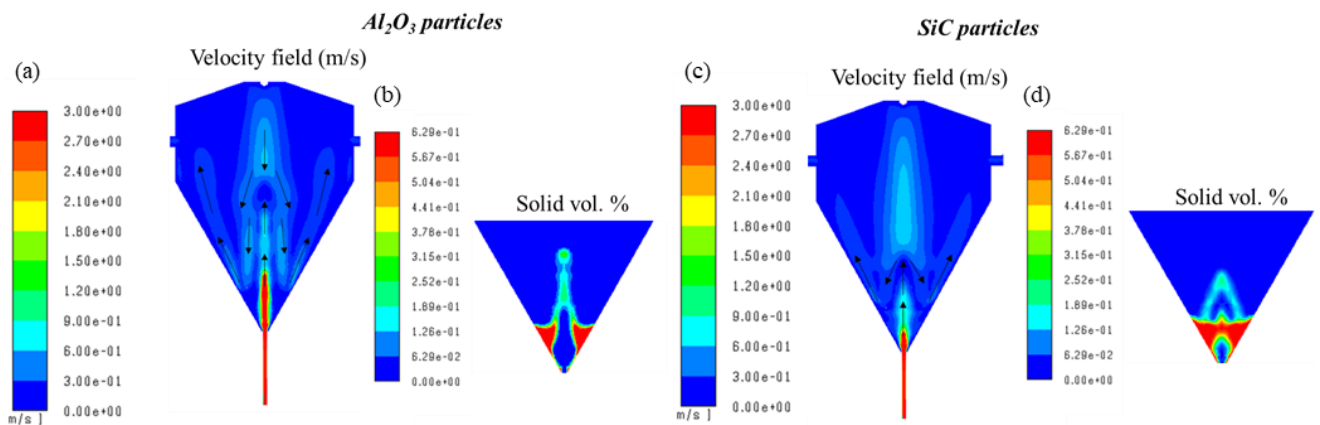
287 Subsequently, the reactor was simulated under real processing conditions (same bottom and upper gas
 288 flow rates as experiments) with a solar power input of 900W (and with 10g of spouted bed mass). The
 289 obtained temperature distribution is presented in Figure 8-a,b for Al_2O_3 and SiC spouted particles. Just as
 290 the two previous hydrodynamic configurations (empty and packed bed), the reactor cavity walls reached
 291 an average temperature of 1230°C. Unlike the empty configuration where the central gas jet reached only
 292 700°C at the conical part of the reactor, the central gas jet when using the spouted particles reached high
 293 temperatures up to 1180°C right away.



295 **Figure 8.** Temperature distribution (gas and solid phases): (a) 125 μm - Al_2O_3 particles; (b) 300 μm -SiC
 296 particles

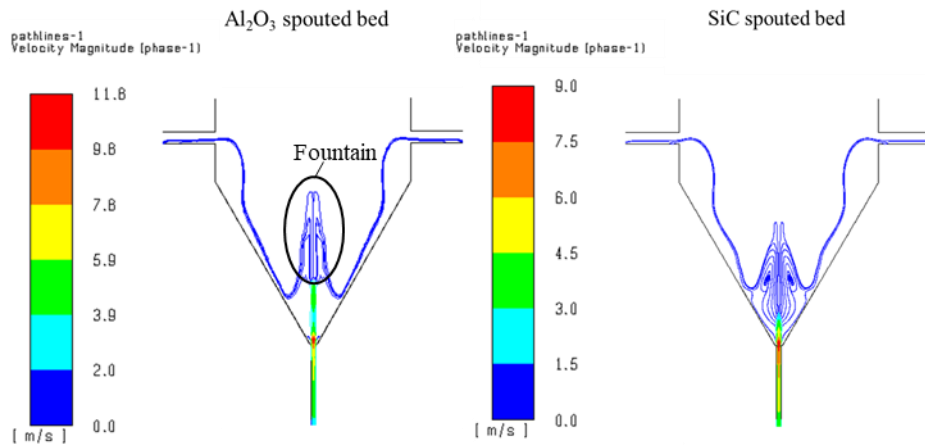
297
 298 By comparing the simulations between Al_2O_3 and SiC, the alumina particles allowed increasing the gas
 299 phase temperature over a larger area. This is because the alumina particles were better spouted thanks to
 300 their lower diameter. Moreover, their temperature was more homogeneously distributed, whereas small
 301 gradients were noticed for SiC particles (Figure 8-b), arising from the less pronounced stirring of the SiC
 302 particles inside the cavity. This is confirmed by the different fountain heights depending on the particles
 303 diameter (Figure 9-b,d). Indeed, the fountain height of the Al_2O_3 bed was two to three times higher than
 304 the fountain height of the SiC particles. Moreover, the central gas flow (bottom jet zone) was more

305 attenuated by the SiC particles that somehow deflected part of the flow towards the annular zone (Figure
 306 9-a,c). For readability reasons, the velocity magnitude field was plotted in a range of 0 m/s to 3 m/s.
 307 However, due to the heating of the gases inside the injection tube, the gas velocity increased from 3 m/s
 308 (at the inlet of the injection tube) to values above 9 m/s at the cone entrance for both 10g beds (Figure
 309 10). This value is hence higher than the minimum spouting velocities (Figures 6 and 7-b); therefore, the
 310 spouting regime was largely achieved with the current experimental flow rates.



311
 312 **Figure 9.** Gas velocity field and solid volume fraction: (a,b) 125 μm -Al₂O₃ particles, (c,d) 300 μm -SiC
 313 particles
 314

315 The spouting gases (Ar+H₂O) pathlines colored by velocity magnitude are presented in Figure 10



316
 317 **Figure 10.** Spouting gases pathlines colored by velocity magnitude
 318

319 It clearly showed that for the Al₂O₃ particles, the flow crosses the bed mainly from its center to reach the
 320 fountain zone while the SiC spouted particles distribute part of the flow towards the annular region.
 321 Thereafter, the spouting gases interact with the upper window inlet flow to get routed all along the cavity
 322 walls towards the gas exit.

323 Overall, the simulations evidenced the benefits of using inert materials in the form of spouted particles to
 324 increase the reaction zone temperature while ensuring an efficient stirring of the particles. The
 325 experimental gas flow rates were high enough to spout the 10g bed. A slight increase of the inlet argon
 326 flow rate is recommended for the largest particles to better disperse them in the upper part of the cavity.
 327 Further increase of the spouting flow rate for the smallest bed particles can possibly impair the process by
 328 entraining them out of the conical cavity. The observed flow instabilities during cold tests for the Al₂O₃
 329 spouted particles were not predicted by the 2D model. They are expected to negatively affect the heat
 330 transfer through the bed at high temperature.

331 A complementary comparative study of the three configurations based on hydrodynamic criteria only is
 332 provided in the Supporting Information, section 3.2.

333

334 **4.2 Experimental study of solar reactor operation**

335 Different experimental runs were performed to study the effect of the inert bed particles on biomass
 336 conversion and syngas composition. The Carbon Conversion Efficiency (CCE), the Cold Gas Efficiency
 337 (CGE) and the Solar-to-Fuel Efficiency (SFE) metrics were used to evaluate the performance of the
 338 reactor for each of the hydrodynamic configurations. The CCE quantifies the extent of biomass
 339 conversion inside the reactor. The CGE is expressed as the ratio between the calorific value of the syngas
 340 over that of the initial biomass. The SFE represents the ratio between the calorific value of syngas over
 341 the total thermal energy that enters the reactor including solar and biomass. For each gas species, the
 342 time-dependent production rate (Q_i) was assessed based on the measured species outlet mole fractions (x_i)
 343 and the inlet inert gas flow rate (Q_{Ar}): ($Q_i = Q_{Ar} \cdot x_i / x_{Ar}$). The averaged syngas mole composition (calculated
 344 over the experiment duration) was determined by integrating the gas production rates over time.

$$345 \quad CCE = \frac{n_C \text{ in syngas}}{n_C \text{ in biomass}} \quad (1)$$

$$346 \quad CGE = \frac{LHV_{\text{syngas}} \cdot m_{\text{syngas}}}{LHV_{\text{feedstock}} \cdot m_{\text{feedstock}}} \quad (2)$$

$$347 \quad SFE = \frac{LHV_{\text{syngas}} \cdot m_{\text{syngas}}}{Q_{\text{solar}} + LHV_{\text{feedstock}} \cdot m_{\text{feedstock}}} \quad (3)$$

348 The tests were carried out under stable solar irradiation (DNI variation less than 10%). To stabilize the
 349 reactor temperature, the incident solar power was controlled by adjusting the opening of a trapdoor
 350 located between the heliostat and the reactor frame. The average solar power directly absorbed by the
 351 cavity through the aperture was $900 \pm 100\text{W}$ to maintain the reactor at 1200°C and $1200 \pm 100\text{W}$ to
 352 maintain the reactor at 1300°C .

353 The experimental conditions at 1200°C (Runs#1-7) and 1300°C (Runs#8-11) are recapped in Table 4.
 354 The calculated $(S/B)/(S/B)_{st}$ mole ratio was equal to 1.24 based on Eq.4 for calculating the $(S/B)_{st}$
 355 stoichiometric ratio (where S denotes steam flow rate including both inlet steam and moisture contained

356 in biomass, and B denotes dry biomass flow rate). Accordingly, the biomass particles were gasified with a
 357 slightly overstoichiometric steam flow rate.

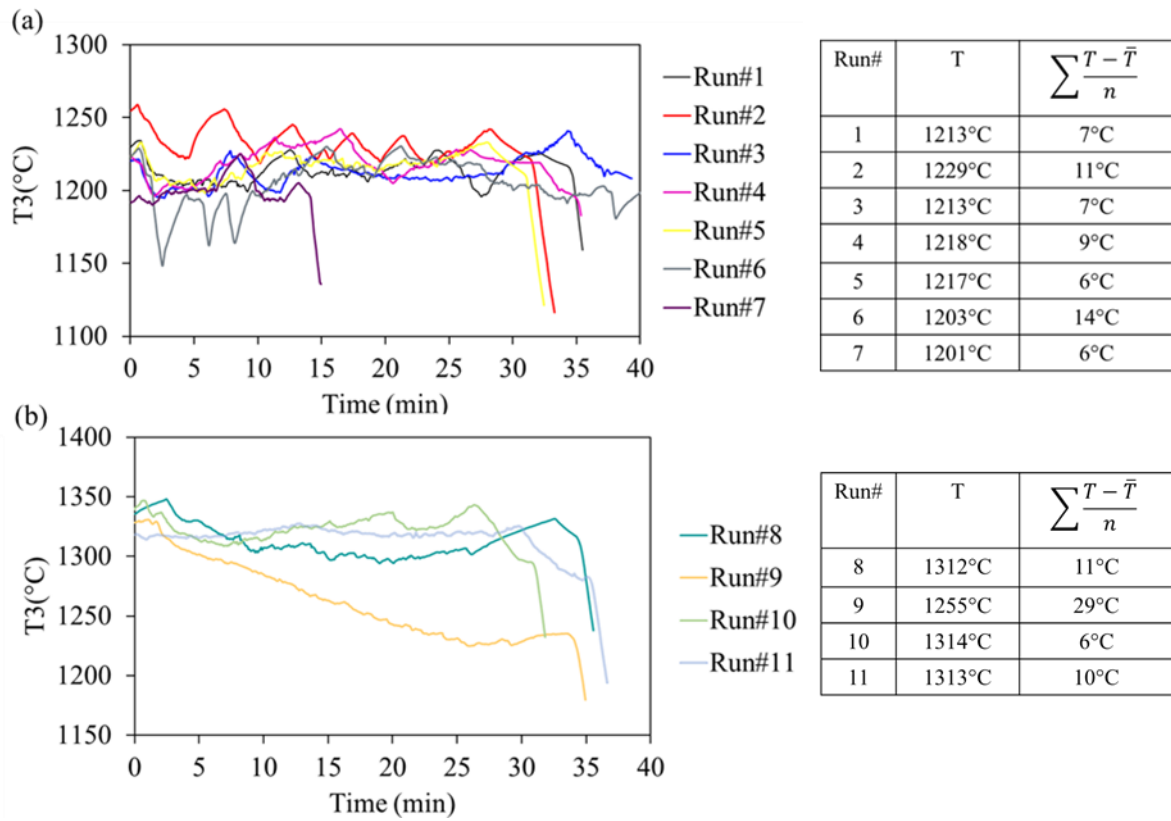


359
 360 **Table 4.** Operating conditions of the directly irradiated reactor (1200 and 1300 °C, 10g of inert materials)

Run#	T _{operating} (°C)	Bed material		Bed configuration	Wood feeding rate (g/min)	Ar flow rate (NL/min)	H ₂ O flow rate (g/min)
		material	size				
1	1200	Empty	-	Dilute spouted bed	1.2	0.2	0.2
2	1200	Al ₂ O ₃	3mm	Packed bed	1.2	0.2	0.2
3	1200	Al ₂ O ₃	125µm	Spouted bed	1.2	0.2	0.2
4	1200	SiC	300µm	Spouted bed	1.2	0.2	0.2
5	1200	SiC	300µm	Spouted bed	1.2	0.3	0.2
6	1200	Olivine	300µm	Spouted bed	1.2	0.2	0.2
7	1200	Sand	300µm	Spouted bed	1.2	0.2	0.2
8	1300	Al ₂ O ₃	3mm	Packed bed	1.2	0.2	0.2
9	1200-1300	Al ₂ O ₃	125µm	Spouted bed	1.2	0.2	0.2
10	1300	Al ₂ O ₃	125µm	Spouted bed	1.2	0.2	0.2
11	1300	SiC	300µm	Spouted bed	1.2	0.2	0.2

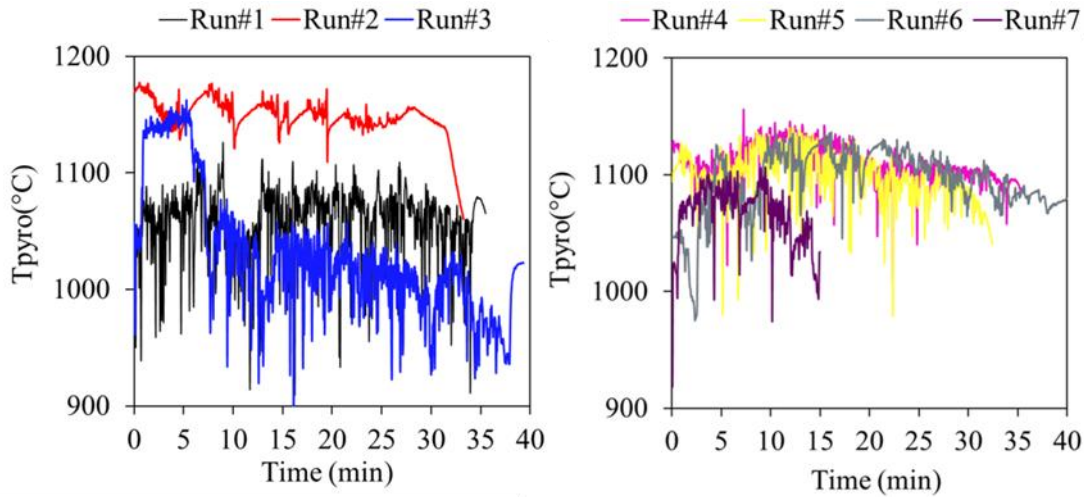
361
 362 After solar tests, the material mass balance was assessed via systematic comparison between the initial
 363 mass of injected reactants (both biomass and water) and the output mass of products (syngas compounds,
 364 excess water and entrained char/soot/tar remaining in bubbler and filters). Overall, the mass balance
 365 closure was above 84% regardless of the experimental runs (as shown in Table SI3). Moreover, no
 366 remaining char was found inside the cavity after tests.

367 The reactor temperature as measured by T3 (inside the cavity) for Runs#1-11 is plotted in Figure 11-a,b.
 368 The temperature was effectively maintained around the set point values (maximum mean deviation of
 369 14°C in Run#6). Due to the insufficient solar heating in Run#9, the reactor temperature could not be
 370 maintained at 1300°C (it declined to values approaching 1200°C) and the mean deviation was therefore
 371 higher (about 29°C).



372
 373 **Figure 11.** T3 measurements for Runs#1-11 at 1200°C and 1300°C (left); Average and mean deviation of
 374 temperature (right)

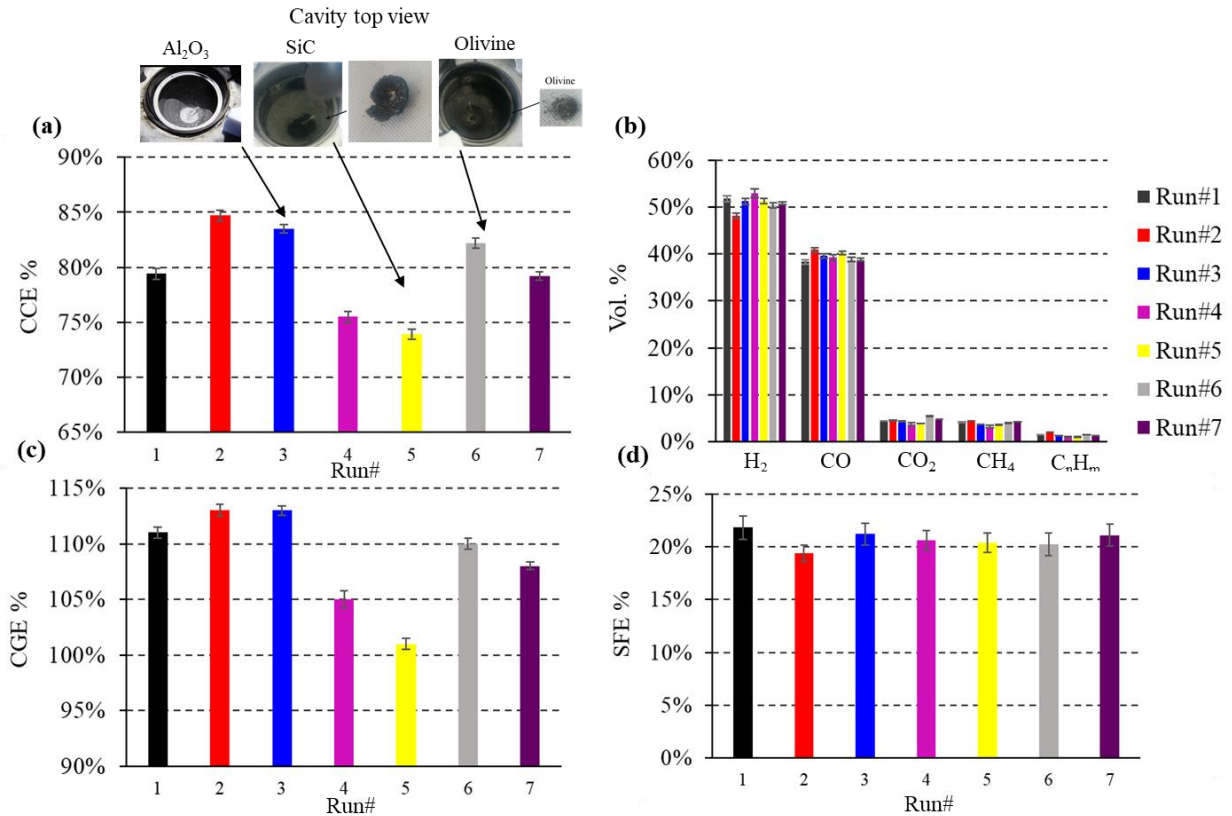
375
 376 Pyrometer measurements (T_{pyro}) in Figure 12 indicated strong fluctuations in temperature for the spouted-
 377 bed configuration because the pyrometer pointed directly at the bed top surface. Given the spouting of
 378 particles (including wood and inert particles) and the continuous feeding of fresh biomass, such
 379 fluctuations given by the optical pyrometer are expected (for simplification, the same emissivity of 1 was
 380 assumed for all the measurements, although in practice the emissivity is dependent on the materials
 381 properties and temperature, which also explains the observed differences in measured temperatures). The
 382 fluctuations, which reflect the intense/effective stirring of the particles, were lowered when the packed
 383 Al_2O_3 particles were used (Run#2).



384
385
386

Figure 12. Pyrometer measurements for Runs#1-7 (1200°C)

387 Figure 13 shows the calculated performance metrics and the gas composition for the different
388 hydrodynamic configurations at 1200°C (Runs#1-7).



389
390 **Figure 13.** (a) CCE and top view of the cavity at the end of the experiments (for Al₂O₃, SiC and Olivine);
391 (b) Gas composition; (c) CGE; (d) SFE (Runs#1-7 at 1200°C)

392
393 The carbon conversion in the empty case (Run#1) reached 79.3% and the syngas produced was
394 essentially composed of H₂ and CO. The H₂ and CO volume fractions were respectively 51.6% and

395 38.3%. The use of the packed and spouted bed of Al_2O_3 particles (Runs#2-3) increased the CCE up to
396 84.7%. In contrast, the CCE declined to 75.5% with the spouted 300- μm SiC (Run#4).

397 The increase of the spouting carrier gas flow rate (from 0.2 NL/min in Run#4 to 0.3 NL/min in Run#5)
398 decreased even more the CCE to 73.9%. While the alumina particles remained intact at the end of the
399 experiments and showed chemical inertness, the SiC bed suffered from sintering and adhered to the cavity
400 walls (Figure 13-a). This can also be due to possible side reactions that may occur between SiC and water
401 (forming either $\text{SiO}_2 + \text{CH}_4$ or $\text{SiO}(\text{g}) + 2\text{H}_2 + \text{CO}$, the former being the most thermodynamically
402 favorable). The expected effect of improving the stirring of SiC particles by increasing the carrier gas
403 flow rate was therefore hardly achieved and only impaired the gas and solid residence times.

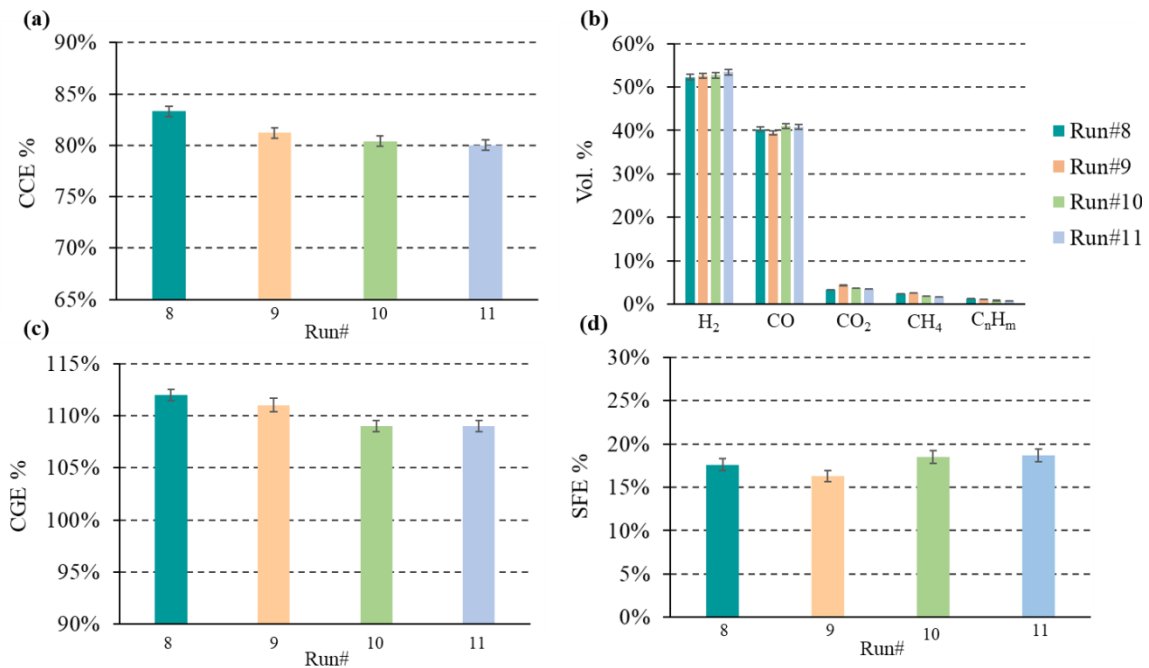
404 The olivine sample in Run#6 also stuck but to a lesser extent on the cavity walls and its color turned from
405 brown/red (due to the presence of iron oxides) to grey (Figure 13-a), suggesting poor chemical inertness
406 at high temperatures. The CCE in Run#6 was still higher than the CCE of the empty cavity and reached
407 82.2%. The silica sand bed in Run#7 was the least resistant material, as the cavity was found almost
408 empty at the end of the experiment, presumably because of the formation of fused silica during spouting
409 caused by particles exposure to high-flux radiation in the upper cavity region. The results in terms of CCE
410 and syngas composition were therefore very similar to Run#1.

411 In general, the bed materials only slightly influenced the gas composition and in all cases, the main
412 syngas components remained H_2 and CO , whereas CO_2 , CH_4 and C_nH_m (mainly C_2H_2) were produced in
413 smaller amounts. The Al_2O_3 particles in Run#2 led to the lowest H_2 concentration (~48.1%) while the
414 light hydrocarbons ($\text{CH}_4 + \text{C}_n\text{H}_m$) volume fraction was the largest (6.4%). The H_2 concentration in Run#4
415 (SiC particles, 0.2 NL/min of spouting carrier gas flow rate) was the highest and reached around 52.9%.
416 This however can be due to the oxidation of SiC by steam, forming additional H_2 in the mixture. The
417 CGE (Figure 13-c) followed a similar pattern as the CCE since the gas composition was only slightly
418 modified by the addition of the inert powders. The peak CGE values were obtained in Runs#2-3 (packed
419 and spouted Al_2O_3 particles) and reached 1.13 against 1.11 in Run#1 (empty cavity). The minimum CGE
420 was 1.01 in Run#5 (SiC bed) when the Ar flow rate was set to 0.3 NL/min.

421 The SFE (Figure 13-d) reached up to 21.8% in Run#1 (empty cavity) and decreased moderately to a
422 minimum value of 19.4% in Run#2 (packed Al_2O_3 particles) even if the CGE was slightly upgraded. The
423 total solar energy consumed (Q_{solar}) for gasifying the 30.0g biomass feedstock was 1.76 ± 0.21 MJ in
424 Run#1. It was higher with inert bed materials: 2.23 ± 0.19 MJ in Run#2 (packed Al_2O_3 particles),
425 2.15 ± 0.24 MJ in Run#3 (spouted Al_2O_3 particles), 1.89 ± 0.21 MJ in Run#4 (spouted SiC particles),
426 1.83 ± 0.19 MJ in Run#5 (spouted SiC particles) and 2.04 ± 0.25 MJ in Run#6 (spouted olivine particles).
427 Q_{solar} in Run#7 was 0.99 ± 0.11 MJ (because only 15.6g of biomass was gasified). While a small increase
428 of Q_{solar} was observed when using the inert particles probably for heating the bed materials, the

429 uncertainty on Q_{solar} makes it difficult to precisely conclude about the influence of the bed materials on
 430 the solar energy consumption and therefore on the SFE.

431 The effect of temperature on the gasification process was studied in Runs#8-11 with the Al_2O_3 packed
 432 particles (Run#8), Al_2O_3 spouted bed particles (Runs#9-10) and with SiC bed (Run#11). Olivine and sand
 433 were not tested at this temperature, due to their low stability and resistance to the solar heating. Figure 14
 434 shows the calculated reactor efficiencies and gas composition at 1300°C.



435
 436 **Figure 14.** (a) CCE; (b) Gas composition; (c) CGE; (d) SFE (Runs#8-11 at 1300°C)

437
 438 The temperature increase showed only a little impact on the CCE and CGE for the packed bed
 439 configuration (Run#8) but the influence on the gas composition was more pronounced. The CCE and the
 440 CGE both slightly declined by less than 1.5% whereas the syngas ($\text{H}_2 + \text{CO}$) concentration was improved
 441 by 4.3% (from Run#2 to Run#8) due to the enhancement of the kinetic rates of the steam methane and
 442 light hydrocarbons reforming ($\text{C}_n\text{H}_m + n\text{H}_2\text{O} \rightarrow (m/2+n) \text{H}_2 + n\text{CO}$).

443 The CCE in the Al_2O_3 spouted bed configuration declined with temperature increase, from 83.5% in
 444 Run#3 to 81.1% in Run#9 and 80.4% in Run#10. This decrease in CCE was ascribed to the more favored
 445 entrainment of the reacting char particles, caused by the lower gas residence time that decreased from
 446 0.54s at 1200°C to 0.51s at 1300°C. Accordingly, the CGE declined in a stepwise fashion in Runs#9-10
 447 to reach 109% in Run#10. Moreover, just as in Run#8, the $\text{H}_2 + \text{CO}$ volume fraction was improved by
 448 3.2% at the expense of a noticeable decrease of the $\text{CH}_4 + \text{C}_n\text{H}_m$ by 28.0% (from Run#3 to Run#10). The
 449 largest $\text{H}_2 + \text{CO}$ volume fraction was achieved with the SiC particles (Run#11) reaching 94.2% against
 450 92.1% in Run#4 (SiC bed-1200°C) with a beneficial effect on the CCE and the GGE that approached

451 values of the Al₂O₃ spouted bed possibly due to their better stirring and absorption of the solar flux at
452 1300°C.

453 For all runs (#8-11), the SFE decreased by more than 10% mainly due to the increase of the solar energy
454 consumption. In fact, the calculated Q_{solar} for Runs#8-11 (1300°C) were higher than in Runs#1-7
455 (1200°C) and were respectively 2.49±0.20 MJ, 2.68±0.22 MJ, 2.25±0.18 MJ, 2.16±0.18 MJ.

456

457 **5. Conclusions**

458 This study focused on solar biomass gasification in a directly-irradiated conical lab-scale reactor and
459 addressed the effect of inert particles on the gasification process. Prior to the experimental study,
460 multiphysics CFD gas-particle flow modelling was developed to explore the impact of inert packed or
461 spouted particles on the reactor thermal and hydrodynamic behavior.

462 (i) The empty conical cavity (no bed materials) is characterized by a high velocity central gas jet that
463 entrains cyclically the char particles inside the cavity. It offers an excellent exposure to solar radiation
464 evidenced by peak char temperature values but low gas residence time in the central cavity region due to
465 high gas velocities.

466 (ii) The packed-bed configuration using inert particles at the bottom of the conical cavity significantly
467 attenuates the gas jet speed at the central zone, broadens the gas streamlines and limits the entrainment of
468 the reacting particles.

469 (iii) The spouted-bed configuration increases the reaction zone temperature and warrants a continuous
470 gas/particles stirring. The finest inert spouted bed particles are more effective in increasing the reaction
471 zone temperature as they are better spatially dispersed.

472 The experimental part of this study examined five different inert bed materials at 1200°C and 1300°C.

473 The empty configuration (no bed materials used), in which only the reacting wood particles are spouted,
474 showed a CCE of 79% and a CGE of 111% at 1200°C. The Al₂O₃ packed and spouted particles both
475 increased the reactor performance, especially the CCE that reached 85% in the packed bed configuration.
476 The SiC bed suffered strongly from sintering and led to the lowest performance with a CCE of 76% and a
477 CGE of 105%. Olivine and silica sand were not thermochemically stable at 1200°C, with global
478 performance equivalent to the empty configuration. The Al₂O₃ beds were the most suitable for the high-
479 temperature process showing good resistance to thermal shocks and chemical inertness. The effect of bed
480 materials on the outlet syngas composition at these temperatures remained very low (less than 7% for H₂).
481 Increasing temperature to 1300°C improved the syngas quality but globally impaired the CCE, CGE and
482 SFE.

483 Future work should focus on the optimization of the bed particles properties. Low density and high
484 absorption are preferable. New reactor configurations using a confiner could also limit particle
485 entrainment that is a major concern for scale up.

486

487 **Acknowledgements**

488 This study was financially supported by ADEME (French Environment and Energy Management
489 Agency).

490

491

492 **References**

493 Bellouard Q., Abanades S., Rodat S., Dupassieux N., 2017a. Solar thermochemical gasification of wood
494 biomass for syngas production in a high-temperature continuously-fed tubular reactor. *Int. J. Hydrog.*
495 *Energy* 42, 13486-13497.

496 Bellouard Q., Abanades S., Rodat S., Dupassieux N., 2017b. Biomass Gasification in an Innovative
497 Spouted-Bed Solar Reactor: Experimental Proof of Concept and Parametric Study. *Energy & Fuels* 31,
498 10933-10945.

499 Bellouard Q., Abanades S., Rodat S., 2018. Design, simulation and experimental study of a directly-
500 irradiated solar chemical reactor for hydrogen and syngas production from continuous solar-driven wood
501 biomass gasification. *Int. J. Hydrog. Energy* 44, 19193-19205.

502 Boujjat, H., Rodat, S., Chuayboon, S., Abanades, S., 2019a. Numerical simulation of reactive gas-particle
503 flow in a solar jet spouted bed reactor for continuous biomass gasification. *Int. J. Heat Mass Transf.* 144,
504 118572.

505 Boujjat, H., Rodat, S., Chuayboon, S., Abanades, S., 2019b. Experimental and numerical study of a
506 directly irradiated hybrid solar/combustion spouted bed reactor for continuous steam gasification of
507 biomass. *Energy* 189, 116118.

508 Chuayboon, S., Abanades, S., Rodat, S., 2018a. Comprehensive performance assessment of a continuous
509 solar-driven biomass gasifier. *Fuel Process. Tech.* 182, 1-14.

510 Chuayboon, S., Abanades, S., Rodat, S., 2018b. Experimental analysis of continuous steam gasification of
511 wood biomass for syngas production in a high-temperature particle-fed solar reactor. *Chem. Eng. &*
512 *Proc.: Proc. Intens.* 125, 253-265.

513 Erkiaga, A., Lopez, G., Amutio, M., Bilbao, J., Olazar, M., 2013. Steam gasification of biomass in a
514 conical spouted bed reactor with olivine and γ -alumina as primary catalysts. *Fuel Process. Technol.* 116,
515 292–299.

516 Gokon, N., Ono, R., Hatamachi, T., Liuyun, L., Kim, H.J., Kodama, H.J., 2012. CO₂ gasification of coal
517 cokes using internally circulating fluidized bed reactor by concentrated Xe-light irradiation for solar
518 gasification. *Int. J. Hydrog. Energy* 37, 12128-12137

519 Gregg, G.W., Taylor, R.W., Campbell, J.H., Taylor, J.R., Cotton, A., 1980. Solar gasification of coal,
520 activated carbon, coke and coal and biomass mixtures. *Sol. Energy* 25, 353-364.

521 Hathaway, B.J., Kittelson, D.B., Davidson, J.H., 2014. Development of a Molten Salt Reactor for Solar
522 Gasification of Biomass. *Energy Procedia* 49, 1950–1959.

523 Higman, C., 2013. State of the Gasification Industry – the Updated Worldwide Gasification Database,
524 Germany.

525 Kodama T., Gokon, N., Enomoto, S., Itoh, S., Hatamachi, T., 2010. Coal Coke Gasification in a
526 Windowed Solar Chemical Reactor for Beam-Down Optics. *J. Sol. En. Eng.* 132(4):041004.

527 Kodama, T., Kondoh, Y., Tamagawa, T., Funatoh, A., Shimizu, K.I., Kitayama, Y., 2002. Experimental
528 investigation of a packed-bed solar reactor for the steam-gasification of carbonaceous feedstocks. *Energy
529 & Fuels* 16, 1264-1270.

530 Kruesi, M., Jovanovic, Z.R., Dos Santos, E.C., Yoon, H.C., Steinfeld, A., 2013. Solar-driven steam-based
531 gasification of sugarcane bagasse in a combined drop-tube and fixed-bed reactor – Thermodynamic,
532 kinetic, and experimental analyses. *Biomass & Bioenergy* 52, 173–183.

533 Li, X., Dai, Y.J., Wang, R.Z., 2015. Performance investigation on solar thermal conversion of a conical
534 cavity receiver employing a beam-down solar tower concentrator. *Sol. Energy* 114, 134–151.

535 Lopez, G., Cortazar, M., Alvarez, J., Amutio, M., Bilbao, J., Olazar, M., 2017. Assessment of a conical
536 spouted with an enhanced fountain bed for biomass gasification. *Fuel* 203, 825–831.

537 Loutzenhiser, P.G., Muroyama, A.P., 2017. A review of the state-of-the-art in solar-driven gasification
538 processes with carbonaceous materials, *Sol. Energy* 156, 93-100.

539 Makibar, J., Aranzazu, R.F-A., Diaz, L., Gartzten, L., Olazar, M., 2012. Pilot scale conical spouted bed
540 pyrolysis reactor: Draft tube selection and hydrodynamic performance. *Powder Technol.*, 219, 49-58.

541 Markowski, A., Kaminski, W., 1983. Hydrodynamic characteristics of jet-spouted beds. *The Canadian J.
542 of Chem. Eng.* 62, 377-381.

543 Mathur, K.B., Gishler, P.E., 1955. A technique for contacting gases with coarse solid particles. *AIChE J.*
544 1,157–164.

545 Müller, F., Poživil, P., Van Eyk, P.J., Villarrazo, A., Haueter, P., 2017. A pressurized high-flux solar
546 reactor for the efficient thermochemical gasification of carbonaceous feedstock. *Fuel* 193, 432–443.

547 Noone, C.J., Torrilhon, M., Mitsos, A., 2012. Heliostat field optimization: A new computationally
548 efficient model and biomimetic layout. *Sol. Energy* 86, 792–803.

549 Olazar, M., San Jose, M.J., Aguayo, A.T., Arandes, J.M., Bilbao, J.; 1992. Stable operation conditions for
550 gas-solid contact regimes in conical spouted beds. *Ind. Eng. Chem. Res.* 31, 1784–1792.

551 Piatkowski, N., Wieckert, C., Steinfeld, A., 2009. Experimental investigation of a packed-bed solar
552 reactor for the steam-gasification of carbonaceous feedstocks. *Fuel Process. Technol.* 90, 360-366.

553 Puig-Arnavat, M., Tora, E.A., Bruno, J.C., Coronas, A., 2013. State of the art on reactor designs for solar
554 gasification of carbonaceous feedstock, *Sol. Energy* 97, 67–84.

555 Safarian, S., Unnpórsson, R., Richter, C., 2019. A review of biomass gasification modelling, *Renew.*
556 *Sustain. Energy Rev.* 110, 378-391.

557 Taylor, R.W., Berjoan, R., Coutures, J.P., 1983. Solar gasification of carbonaceous materials, *Sol. Energy*
558 30, 513–525.

559 Z'Graggen, A., Haueter, P., Trommer, D., Romero, M., De Jesus, J.C., Steinfeld, A., 2006. Hydrogen
560 production by steam-gasification of petroleum coke using concentrated solar power—II Reactor design,
561 testing, and modeling. *Int. J. Hydrog. Energy*, vol. 31, no. 6, pp. 797–811, 2006.

562

563